AIAA JOURNAL
Vol. 48, No. 3, March 2010

Simulation of Turbulent Mixing Behind a Strut Injector in Supersonic Flow

Franklin Génin* and Suresh Menon†
Georgia Institute of Technology, Atlanta, Georgia 30332-0150

DOI: 10.2514/1.43647

The flowfield downstream of a strut-based injection system in a supersonic combustion ramjet is investigated using large-eddy simulation with a new localized dynamic subgrid closure for compressible turbulent mixing. Recirculations are formed at the base of the strut in the nonreacting flow and trap some of the injected fluid. The high levels of turbulence along the underexpanded hydrogen jets and in the shear layer lead to a high level of mixing of fuel and freestream fluids. Furthermore, the shear layer unsteadiness permits efficient large-scale mixing of freestream and injected fluids. In the reacting flowfield, the flame anchoring mechanism is, however, found to depend more on a recirculation region located downstream of the injectors than on their sides. A region of reverse flow is formed that traps hot products and radicals. Intermittent convection of hot fluid toward the injector occurs and preheats the reactants.

Nomenclature

E	=	total energy, $m^2\ s^{-2}$
ER	=	equivalence ratio
F	=	flux vector
M	=	Mach number
MW	=	molecular weight, $kg\ mol^{-1}$
N_s	=	number of species considered in the simulation
P	=	pressure, $kg\ m^{-1}\ s^{-2}$
Pr	=	Prandtl number
Q	=	vector of conserved variables
R	=	mixture gas constant, $m^2\ s^{-2}\ K^{-1}$
S	=	strain rate tensor, s^{-1}
Sc	=	Schmidt number
V	=	diffusion velocity, $m\ s^{-1}$
Y_k	=	mass fraction of species, k
$\mathcal{C}$	=	mixture gas constant-temperature correlation, $m^2\ s^{-2}$
$\mathcal{D}$	=	dissipation of kinetic energy, $kg\ m^{-1}\ s^{-3}$
$\mathcal{E}$	=	mass fraction-internal energy correlation, $m^2\ s^{-2}$
$\mathcal{H}$	=	enthalpy-velocity correlation, $kg\ s^{-3}$
$\mathcal{L}$	=	Leonard stress, $kg\ m^{-1}\ s^{-2}$
$\mathcal{P}$	=	production of kinetic energy, $kg\ m^{-1}\ s^{-3}$
$\mathcal{R}_u$	=	universal gas constant, $kg\ m^2\ mol^{-1}\ s^{-2}\ K^{-1}$
$\mathcal{T}$	=	diffusion of kinetic energy, $kg\ m^{-1}\ s^{-3}$
c_ϵ	=	closure coefficient for the k^{sgs} dissipation
c_v	=	closure coefficient for the turbulent viscosity
c_p	=	specific heat at constant pressure, $m^2\ s^{-2}\ K^{-1}$
c_v	=	specific heat at constant volume, $m^2\ s^{-2}\ K^{-1}$
e	=	internal energy, $m^2\ s^{-2}$
k^{sgs}	=	subgrid kinetic energy, $m^2\ s^{-2}$
pd	=	pressure dilatation correlation, $kg\ m^{-1}\ s^{-3}$
q_i	=	heat-flux vector, $kg\ s^{-3}$
t	=	time, s
u_i	=	velocity component in Cartesian coordinates, $m\ s^{-1}$
x_i	=	Cartesian coordinate, m
Δ	=	grid size and characteristic lengthscale, m
δ_{ij}	=	Kronecker symbol
θ	=	mass fraction-diffusion velocity correlation, $kg\ m^{-2}\ s^{-1}$
λ	=	switch function
ρ	=	density, $kg\ m^{-3}$
σ	=	viscous work, $kg\ s^{-3}$
τ_{ij}	=	stress tensor, $kg\ m^{-1}\ s^{-2}$

Subscripts

i	=	index indicating the Cartesian direction ($i = 1, 2, 3$)
j	=	index indicating the Cartesian direction ($j = 1, 2, 3$)
k	=	index indicating the species ($k = 1, .., N_s$)
α_{pd}	=	closure coefficient for the pressure dilatation

Superscripts

$\bar{}$	=	spatially filtered variable
$\tilde{}$	=	Favre-averaged variable
s	=	central flux computation
sgs	=	subgrid-scale level
test	=	test-scale level
u	=	upwind flux computation
$\langle\,\rangle$	=	explicitly filtered variable

I. Introduction

DEVELOPMENT of advanced propulsion engines for high-speed flights requires both experimental and numerical studies to interlace and provide supporting formation and/or guidance for design. However, the results of computational simulations usually provide no more than guidelines to the design of experimental rigs and the overall goal of using a numerical predictive capability to simulate actual flight conditions still remains unreached. A valid, accurate, and trustworthy numerical strategy will require development and validation of submodels to simulate turbulent mixing, shock-shear interactions, and combustion under realistic conditions. Although Reynolds-averaged Navier–Stokes (RANS) models have been used for some time, many of the critical processes are highly unsteady and therefore, a time-accurate method such as large-eddy simulation (LES) is probably most likely to be a realistic option. However, for a practical LES approach to be useful for the study of such flows, further advancement in numerical algorithms, subgrid closures, and a highly efficient parallel simulation strategy are required. In this paper we describe the development of an LES methodology that addresses some of these objectives.

Presented as Paper 132 at the 47th AIAA Aerospace Sciences Meeting Including The New Horizons Forum and Aerospace Exposition, Orlando, FL, 5–8 January 2009; received 4 February 2009; revision received 3 June 2009; accepted for publication 10 September 2009.

*Graduate Research Assistant, School of Aerospace Engineering; franklin.genin@gmail.com.

†Professor, School of Aerospace Engineering; suresh.menon@gatech.edu. Associate Fellow AIAA.

The numerical scheme employed for the resolution of turbulence in supersonic flows is critical to the reliability of the simulation. In the context of direct simulations or large-eddy simulations with explicit subgrid modeling, low-dissipation schemes are used to properly capture turbulent structures. These schemes are, however, poorly suited to the capture of shock waves and other flow discontinuities. Higher order schemes for the resolution of high-speed flows, on the other hand, can efficiently capture such discontinuities as a part of the solution, but behave poorly in turbulent regions. To circumvent this issue, several methodologies have been developed. Artificial dissipation and artificial diffusion techniques [1–4] are designed to add an explicit dissipation/diffusion to the numerical resolution. This additional term in the governing equations is triggered by some sort of flow smoothness detection algorithm, and acts mostly in regions of stronger discontinuities. Hybrid schemes, on the other hand, combine two schemes with different characteristics within one numerical algorithm, and blend or switch between flux evaluations [5–9]. The governing equations are not modified to stabilize the numerical resolution, but rather the built-in dissipation of the shock-capturing scheme permits the proper resolution of the flow discontinuities.

Another major requirement for a successful LES of high-speed flows resides in the development of advanced and reliable closure models. A large amount of work has been devoted to the development of RANS methods for various flow conditions, in particular for supersonic flows. Developments in LES closures for high-speed flows are more recent and more limited. In compressible flows, turbulence can be decomposed into solenoidal and dilatational contributions. The first contribution is found in incompressible flows, and involves the interaction of vortical structures through nonlinearities and viscous forces. This regime is characterized by the energy cascade. The second contribution is specific to compressible turbulence and is an ondulatory and propagative mode, where kinetic energy is exchanged with the energy contained in the thermodynamics fluctuations. Many models based on incompressible closures have integrated modeling terms for the dilatational dissipation and pressure dilatation correlation to account for the second mode. It has been shown [10], however, that the compressible part of the turbulent field remains small as long as the turbulent Mach numbers is small. Furthermore, high values for the turbulent Mach number are not encountered in high-speed boundary and free-shear layers, unless hypersonic speeds are considered [10–12]. When shock waves interact with turbulent fields, however, the compressible portion of the turbulent field in the postshock region might be more significant. However, the energy mode redistribution toward the solenoidal turbulence quickly relaxes this energy distribution.

In the present paper, we describe the development of a robust hybrid algorithm that can simulate unsteady shock motions as well as turbulent shear flows in complex configurations using a generalized multiblock structured grid solver. To capture shock-shear interactions in high Mach number LES, we also describe a dynamic subgrid closure approach that explicitly takes into account the effect of compressibility on the turbulent field. This LES methodology is applied to the study of a strut-based injection system for Scramjet chambers. The configuration studied here reproduces the facility used in experimental studies at the DLR, German Aerospace Center for both cold and reactive flows [13–15]. This experimental facility has also been studied numerically by several researchers [16–20].

II. Governing Equations and Numerical Algorithm

A. LES Equations

We denote $\bar{f}$ the spatially filtered variable f, $\tilde{f}$ the Favre-filtered, or density-filtered, variable f defined as $\tilde{f} = \overline{\rho f}/\bar{\rho}$, where ρ represents the local fluid density. The compressible LES equations for mass, momentum, total energy, and species densities conservation are

$$\frac{\partial \bar{\rho}}{\partial t} + \frac{\partial \bar{\rho}\tilde{u}_i}{\partial x_i} = 0 \tag{1}$$

$$\frac{\partial \bar{\rho}\tilde{u}_i}{\partial t} + \frac{\partial}{\partial x_j}[\bar{\rho}\tilde{u}_i\tilde{u}_j + \bar{P}\delta_{ij} - \bar{\tau}_{ij} + \tau_{ij}^{\mathrm{sgs}}] = 0 \tag{2}$$

$$\frac{\partial \bar{\rho}\tilde{E}}{\partial t} + \frac{\partial}{\partial x_i}[(\bar{\rho}\tilde{E} + \bar{P})\tilde{u}_i + \bar{q}_i - \tilde{u}_j\bar{\tau}_{ij} + \mathcal{H}_i^{\mathrm{sgs}} + \sigma_i^{\mathrm{sgs}} + q_i^{\mathrm{sgs}}] = 0 \tag{3}$$

$$\frac{\partial \bar{\rho}\tilde{Y}_k}{\partial t} + \frac{\partial}{\partial x_i}[\bar{\rho}(\tilde{Y}_k\tilde{u}_i + \tilde{Y}_k\tilde{V}_{i,k}) + \mathcal{Y}_{i,k}^{\mathrm{sgs}} + \theta_{i,k}^{\mathrm{sgs}}] = \overline{\dot{\omega}_k} \qquad k = 1, \ldots, N_s \tag{4}$$

In these equations, the velocity vector in Cartesian coordinates is denoted by $(u_i)_{i=1,2,3}$, P is the pressure, and Y_k is the mass fraction for species k. Also, N_s is the total number of species in the flow. The unfiltered total energy of the system E is the sum of kinetic and internal energies. As a consequence, the filtered total energy $\tilde{E}$ is given as the sum of the filtered internal energy $\tilde{e}$, the resolved kinetic energy $(1/2)[\tilde{u}_i\tilde{u}_i]$, and the subgrid kinetic energy $k^{\mathrm{sgs}} = (1/2)[\widetilde{u_i u_i} - \tilde{u}_i\tilde{u}_i]$.

A perfect gas equation of state is assumed here to close the relation between primitive and conservative variables. This filtered equation of state is $\bar{P} = \bar{\rho}(\tilde{R}\tilde{T} + \mathcal{C}^{\mathrm{sgs}})$, where T is the flow temperature $\mathcal{C}^{\mathrm{sgs}} = \widetilde{RT} - \tilde{R}\tilde{T}$, R the mixture gas constant obtained from the species molecular weights $(\mathrm{MW}_k)_{k=1,\ldots,NS}$, and R_u the universal gas constant, as

$$R = \sum_{k=1,\ldots,NS} Y_k \frac{\mathcal{R}_u}{\mathrm{MW}_k} \tag{5}$$

The filtered internal energy per unit mass is then given by

$$\tilde{e} = \sum_{k=1,\ldots,NS} \widetilde{Y_k e_k} = \sum_{k=1,\ldots,NS} \tilde{Y}_k \int_0^{\tilde{T}} c_{v,k}(T)\mathrm{d}T + \sum_{k=1,\ldots,NS} \mathcal{E}_k^{\mathrm{sgs}} \tag{6}$$

where $\mathcal{E}_k^{\mathrm{sgs}} = \widetilde{Y_k e(T)} - \tilde{Y}_k e(\tilde{T})$, and the filtered enthalpy $\tilde{h}$ is defined as $\bar{\rho}\tilde{h} = \bar{\rho}\tilde{e} + \bar{P}$ and, for perfect gases, can be expressed as

$$\tilde{h} = \sum_{k=1,\ldots,NS} \tilde{Y}_k \int_0^{\tilde{T}} c_{p,k}(T)\mathrm{d}T + \sum_{k=1,\ldots,NS} \mathcal{E}_k^{\mathrm{sgs}} + \mathcal{C}^{\mathrm{sgs}} \tag{7}$$

where $c_{p,k} = c_{v,k} + R_k$. The temperature dependence of the specific heat at constant pressure for the kth species $c_{p,k}$ is approximated using a polynomial of order 4, obtained from experimental temperature curve fits [21]. The filtered viscous stress tensor $\bar{\tau}_{ij}$ is computed based on the filtered strain rate $\tilde{S}_{ij}$, and the filtered heat-flux vector $\bar{q}_i$ is evaluated using a Fourier law. The viscosity and thermal conductivity of each species are computed using polynomial curve fits for the temperature dependence, and the mixture transport properties are evaluated from the individual species properties using Wilke's formulation [22]. Finally, the filtered diffusion velocity for the kth species $\tilde{V}_{i,k}$ is modeled using Fick's law. The diffusion coefficients for each species are computed using a constant, but species specific, Lewis number formulation.

The governing equations for LES have been obtained by application of a spatial filter onto the Navier–Stokes equations, separating the larger, geometry-dependent scales of motion from the universal small scales. All the subgrid-scale terms, denoted with an *sgs* superscript in the governing Eqs. (1–4), represent the statistics of the turbulent field at scales smaller than the local grid size and are unclosed. A modeling approach is required to evaluate the subgrid stress τ_{ij}^{sgs}, subgrid viscous work σ_i^{sgs}, subgrid enthalpy flux $\mathcal{H}_i^{\mathrm{sgs}}$, subgrid diffusion of energy due to species-diffusion q_i^{sgs}, subgrid species flux $\mathcal{Y}_{i,k}^{\mathrm{sgs}}$, subgrid species-diffusion velocity correlation $\theta_{i,k}^{\mathrm{sgs}}$, subgrid mixture gas constant-temperature correlation $\mathcal{C}^{\mathrm{sgs}}$, and subgrid mass fraction-internal energy correlation $\mathcal{E}_k^{\mathrm{sgs}}$. The present methodology is presented next.

B. Subgrid Closure Model

Modeling the unresolved statistics of turbulence and their impact on the flow evolution can be achieved through various approaches, and many turbulence models [23] can be found in the literature. In particular, two very different conceptual approaches are commonly

found in the studies of turbulent flows, namely the use of implicit LES formulation vs explicit methods. In the former method, the use of higher order upwind schemes is associated with numerical dissipation that mimics the subgrid-scale behavior, whereas the latter method is based on the use of low-dissipation numerical schemes with explicit models for the subgrid behavior. Implicit LES [24,25] have gained popularity in the studies of high-speed turbulent flows, as the need for shock-capturing schemes makes the numerical dissipation unavoidable. In the present study, however, the resolution of the LES equations is performed using a hybrid scheme that uses a shock-capturing methodology in discontinuity regions only, and reverts to a low-dissipation scheme away from the hydrodynamic jumps. In this context an explicit closure is needed, and the present approach is based on a gradient diffusion approach, using an eddy viscosity formulation.

1. Closure Formulation

Given the eddy viscosity ν_t, the subgrid stress τ_{ij}^{sgs} in the momentum equation is modeled as

$$\tau_{ij}^{\text{sgs}} = -2\bar{\rho}\nu_t\left(\tilde{S}_{ij} - \frac{1}{3}\tilde{S}_{kk}\delta_{ij}\right) + \frac{2}{3}k^{\text{sgs}}\delta ij \tag{8}$$

The two unclosed terms in the energy equation $\mathcal{H}_i^{\text{sgs}}$ and σ_i^{sgs} are modeled together as

$$\mathcal{H}_i^{\text{sgs}} + \sigma_i^{\text{sgs}} = -(\bar{\rho}\nu_t + \mu)\frac{\partial k^{\text{sgs}}}{\partial x_i} - \frac{\bar{\rho}\nu_t c_p}{Pr_t}\frac{\partial \tilde{T}}{\partial x_i} + \tilde{u}_j\tau_{ij}^{\text{sgs}} \tag{9}$$

The subgrid diffusion of species mass fractions $\mathcal{Y}_{i,k}^{\text{sgs}}$ is also modeled using an eddy-diffusivity assumption, as

$$\mathcal{Y}_{i,k}^{\text{sgs}} = -\frac{\bar{\rho}\nu_t}{Sc_t}\frac{\partial \tilde{Y}_k}{\partial x_i} \tag{10}$$

The other unclosed terms $\theta_{i,k}^{\text{sgs}}$, $q_{i,k}^{\text{sgs}}$, C^{sgs}, and $\mathcal{E}_k^{\text{sgs}}$ are often neglected in conventional LES studies [26,27], and are neglected for the problems of interest here. Their significance might need to be revisited later.

The characteristic length and velocity scales used to define the eddy viscosity are provided by the local grid size $\bar{\Delta}$ and the subgrid kinetic energy k^{sgs}, respectively, and $\nu_t = c_\nu\bar{\Delta}\sqrt{k^{\text{sgs}}}$. $\bar{\Delta}$ is computed as the cubic root of the cell volume, but this definition is sometimes revisited for high-aspect ratio cells. In the present study, a dynamic evaluation of the closure coefficients is employed, which makes the actual definition of $\bar{\Delta}$ irrelevant. The ratio between test-scale (defined later) and local grid sizes is more relevant. The subgrid kinetic energy is obtained from a transport model. The local value of subgrid kinetic energy depends on the convection, diffusion $\mathcal{T}_{k^{\text{sgs}}}$, production $\mathcal{P}_{k^{\text{sgs}}}$, dissipation of k^{sgs} $\mathcal{D}_{k^{\text{sgs}}}$, and on the subgrid pressure dilatation correlation $pd_{k^{\text{sgs}}}$

$$\frac{\partial}{\partial t}\bar{\rho}k^{\text{sgs}} + \frac{\partial}{\partial x_i}(\bar{\rho}\tilde{u}_i k^{\text{sgs}}) = \mathcal{T}_{k^{\text{sgs}}} + pd_{k^{\text{sgs}}} + \mathcal{P}_{k^{\text{sgs}}} - \mathcal{D}_{k^{\text{sgs}}} \tag{11}$$

The production of k^{sgs}, $\mathcal{P}_{k^{\text{sgs}}} = -\tau_{ij}^{\text{sgs}}\partial\tilde{u}_i/\partial x_i$, is readily available with the model for τ_{ij}^{sgs} described earlier. The dissipation of subgrid kinetic energy is evaluated based on the characteristic length and velocity scales of subgrid turbulence as $\mathcal{D}_{k^{\text{sgs}}} = \bar{\rho}c_\epsilon(k^{\text{sgs}})^{3/2}/\bar{\Delta}$, in analogy with the Kolmogorov concept of energy cascade. This expression models the total dissipation, modeling both solenoidal and dilatational contributions with the same closure expression. This approximation remains acceptable as long as the turbulent Mach number remains small so that dilatational dissipation remains very small, which is a reasonable assumption in the context of supersonic flows, as reported earlier [10–12].

The diffusion of k^{sgs} is due to subgrid fluctuations in kinetic energy, subgrid fluctuations in viscous stresses, and subgrid fluctuations in pressure. The first contribution (often referred to as the triple-velocity correlation) and the second are modeled together using a k^{sgs} gradient diffusion approach. It has been shown, however, that the diffusion of turbulent kinetic energy due to pressure fluctuations is important in regions of shock/turbulence interaction [9,28,29]. This term contributes to the amplification of turbulent levels in the postshock region and is also closed in the present approach. Using the definition of Favre-averaging along with an eddy-diffusivity assumption, the diffusion of k^{sgs} due to subgrid pressure fluctuations is modeled as

$$\overline{u_i P} - \tilde{u}_i\bar{P} = \bar{\rho}\,\tilde{R}(\widetilde{u_i T} - \tilde{u}_i\tilde{T}) = -\frac{\bar{\rho}\nu_t\tilde{R}}{Pr_t}\frac{\partial \tilde{T}}{\partial x_i} \tag{12}$$

The pressure dilatation correlation is often neglected in models developed for incompressible or low-compressibility flows, but its behavior and contribution to compressible turbulent flows needs to be examined. The study of Ristorcelli [10] shows that, in the small turbulent Mach number regime, this term varies with the square of the turbulent Mach number and depends on the departure from equilibrium. The closure formulation based on the previously cited scaling analysis reads

$$\text{pd}_{k^{\text{sgs}}} = \alpha_{\text{pd}}M_t^{\text{sgs}2}\left(\frac{\bar{\rho}\,\tilde{S}\,k^{\text{sgs}}}{\mathcal{D}_{k^{\text{sgs}}}}\right)^2(\mathcal{P}_{k^{\text{sgs}}} - \mathcal{D}_{k^{\text{sgs}}}) \tag{13}$$

where $M_t^{\text{sgs}2}$ is the turbulent Mach number based on k^{sgs} and $\tilde{S}^2 = \frac{1}{2}\tilde{S}_{ij}\tilde{S}_{ij}$. The final form of the evolution equation for the subgrid kinetic energy is finally obtained as

$$\begin{aligned}\frac{\partial}{\partial t}\bar{\rho}k^{\text{sgs}} + \frac{\partial}{\partial x_i}(\bar{\rho}\tilde{u}_i k^{\text{sgs}}) &= \frac{\partial}{\partial x_i}\left[(\bar{\rho}\nu_t + \mu)\frac{\partial k^{\text{sgs}}}{\partial x_i} + \frac{\bar{\rho}\nu_t\tilde{R}}{Pr_t}\frac{\partial \tilde{T}}{\partial x_i}\right] \\ &\quad - \left[1 + \alpha_{\text{pd}}M_t^{\text{sgs}2}\left(\frac{\bar{\rho}\,\tilde{S}\,k^{\text{sgs}}}{\mathcal{D}_{k^{\text{sgs}}}}\right)^2\right]\left(\tau_{ij}^{\text{sgs}}\frac{\partial\tilde{u}_j}{\partial x_i} + \bar{\rho}c_\epsilon\frac{(k^{\text{sgs}})^{3/2}}{\bar{\Delta}}\right)\end{aligned} \tag{14}$$

2. Localized Dynamic Closure for Subgrid Model Coefficients

The closures of the LES and k^{sgs} equations use five coefficients $(c_\nu, c_\epsilon, Pr_t, Sc_t, \alpha_{\text{pd}})$. Nominal values for these coefficients have been advanced in the past [30]. In the present study, a dynamic evaluation of the coefficients is performed based on the framework of the localized dynamic k^{sgs} model (LDKM [31]). Using the experimental observation of similarity between subgrid stresses τ_{ij}^{sgs} and the Leonard stresses of the explicitly filtered velocity field $\mathcal{L}_{ij}$ [32], a similarity model of the form $\tau_{ij}^{\text{sgs}} = C\mathcal{L}_{ij}$ was suggested, but was found to be unstable. Here, this observation is extended and it is assumed that the stress at the test-filter level [expressed similar to the form in Eq. (8), but with all properties evaluated at the test-filter level] is also similar to the Leonard stress, that is, $\tau_{ij}^{\text{test}} = C_L\mathcal{L}_{ij}$. Noting $\langle f\rangle$ the explicit application of a top-hat test filter of size $\hat{\Delta}$ ($\hat{\Delta} = 2\bar{\Delta}$) performed on variable f, a relation between $\mathcal{L}_{ij}$ and τ_{ij}^{test} is obtained (with $C_L = 1$). The Leonard stress is

$$\mathcal{L}_{ij} = \langle\bar{\rho}\rangle\left(\frac{\langle\bar{\rho}\tilde{u}_i\tilde{u}_j\rangle}{\langle\bar{\rho}\rangle} - \frac{\langle\bar{\rho}\tilde{u}_i\rangle}{\langle\bar{\rho}\rangle}\frac{\langle\bar{\rho}\tilde{u}_i\rangle}{\langle\bar{\rho}\rangle}\right) \tag{15}$$

and is known at the test-filter level. Thus, modeling τ_{ij}^{test} as in Eq. (8), but at the test-filter level, the relation $\tau_{ij}^{\text{test}} = C_L\mathcal{L}_{ij}$ results in

$$\mathcal{L}_{ij} = -2\langle\bar{\rho}\rangle c_\nu\sqrt{k^{\text{test}}}\hat{\Delta}\left(\frac{\langle\bar{\rho}\tilde{S}_{ij}\rangle}{\langle\bar{\rho}\rangle} - \frac{1}{3}\frac{\langle\bar{\rho}\tilde{S}_{kk}\rangle}{\langle\bar{\rho}\rangle}\delta_{ij}\right) + \frac{2}{3}\langle\bar{\rho}\rangle k^{\text{test}}\delta_{ij} \tag{16}$$

so that this relation has c_ν as the only remaining unknown. Using a least-square method [33], c_ν is given by

$$c_\nu = -\frac{\mathcal{M}_{ij}\mathcal{L}'_{ij}}{2\mathcal{M}_{ij}\mathcal{M}_{ij}} \tag{17}$$

where $\mathcal{M}_{ij} = \sqrt{k^{\text{test}}}\hat{\Delta}(\langle\bar{\rho}\tilde{S}_{ij}\rangle - \frac{1}{3}\langle\bar{\rho}\tilde{S}_{kk}\rangle\delta_{ij})$ and $\mathcal{L}'_{ij} = \mathcal{L}_{ij} - \frac{2}{3}\langle\bar{\rho}\rangle k^{\text{test}}\delta ij$. It can be seen that $\mathcal{M}_{ij}$ is fully resolved at the test-

filter level and, therefore, is well defined and not subject to numerical ill-conditioning.

The exact expression for the dissipation of k^{test} is

$$\mathcal{D}_{k^{\text{test}}} = \left\langle (\bar{\tau}_{ij} - \tau_{ij}^{\text{sgs}}) \frac{\partial \tilde{u}_j}{\partial x_i} \right\rangle - \langle (\bar{\tau}_{ij} - \tau_{ij}^{\text{sgs}}) \rangle \frac{1}{\langle \bar{\rho} \rangle} \left\langle \bar{\rho} \frac{\partial \tilde{u}_j}{\partial x_i} \right\rangle \tag{18}$$

Using the similarity assumption, the dissipation of k^{test} is modeled similar to the model for the dissipation of k^{sgs} so that $\mathcal{D}_{k^{\text{test}}} = \langle \bar{\rho} \rangle c_\epsilon (k^{\text{test}})^{3/2} / \hat{\Delta}$. Here again, only the closure coefficient remains unknown. The closure coefficient c_ϵ is then determined as

$$c_\epsilon = \frac{\hat{\Delta}}{\langle \bar{\rho} \rangle (k^{\text{test}})^{\frac{3}{2}}} \left((\mu + \mu_t) \left[\left\langle \tilde{\Sigma}_{ij} \frac{\partial \tilde{u}_j}{\partial x_i} \right\rangle - \frac{1}{\langle \bar{\rho} \rangle} \langle \tilde{\Sigma}_{ij} \rangle \left\langle \bar{\rho} \frac{\partial \tilde{u}_j}{\partial x_i} \right\rangle \right] - \frac{2}{3} \left[\left\langle \bar{\rho} k^{\text{sgs}} \frac{\partial \tilde{u}_k}{\partial x_k} \right\rangle - \frac{1}{\langle \bar{\rho} \rangle} \langle \bar{\rho} k^{\text{sgs}} \rangle \left\langle \bar{\rho} \frac{\partial \tilde{u}_k}{\partial x_k} \right\rangle \right] \right) \tag{19}$$

where Σ_{ij} is twice the traceless strain tensor $\tilde{\Sigma}_{ij} = 2(\tilde{S}_{ij} - \frac{1}{3}\tilde{S}_{kk}\delta_{ij})$.

For compressible flows, the turbulent Prandtl number should also be computed dynamically and locally [34]. At the test-filter level, the expression for the test-scale temperature/velocity correlation can be expressed exactly, and the overspecified system is again solved using a least-square method, leading to a final expression

$$1/Pr_t = -\frac{d_i n_i}{d_i d_i} \tag{20}$$

where

$$d_i = c_v \sqrt{k^{\text{test}}} \hat{\Delta} \frac{1}{\langle \bar{\rho} \rangle} \left\langle \bar{\rho} \frac{\partial \tilde{T}}{\partial x_i} \right\rangle \tag{21}$$

$$n_i = \frac{\langle \bar{\rho} \tilde{u}_i \tilde{T} \rangle}{\langle \bar{\rho} \rangle} - \frac{\langle \bar{\rho} \tilde{u}_i \rangle}{\langle \bar{\rho} \rangle} \frac{\langle \bar{\rho} \tilde{T} \rangle}{\langle \bar{\rho} \rangle} \tag{22}$$

Finally, the pressure dilatation correlation is also evaluated at the test-scale level so that the model coefficient is estimated as

$$\alpha_{\text{pd}} = \frac{\langle \bar{P} \frac{\partial \tilde{u}_i}{\partial x_i} \rangle - \langle \bar{P} \rangle \langle \bar{\rho} \frac{\partial \tilde{u}_i}{\partial x_i} \rangle / \langle \bar{\rho} \rangle}{M_t^{\text{test2}} (\langle \bar{\rho} \tilde{S} \rangle k^{\text{test}} / D_{k^{\text{test}}})^2 (P_{k^{\text{test}}} - D_{k^{\text{test}}})} \tag{23}$$

The denominator depends on the departure from equilibrium at the test-scale level. If the production of k^{test} balances the dissipation, the formulation is ill-posed. The pressure dilatation correlation is expected to be relatively small in most case, reaching 10% of the global dissipation in flow configurations strongly out of equilibrium [10]. For the analysis conducted here, the value of α_{pd} is clipped to prevent divergent values of the modeled pressure dilatation correlation. However, all the other coefficients are allowed to achieve local values without averaging or clipping.

In the present study, the closure coefficient for the subgrid diffusion of species, the turbulent Schmidt number Sc_t, is taken to be a constant. For high Reynolds number flows where the turbulent diffusion of species is dominated by the vortical structures of the flow, the value of the turbulent Schmidt number remains close to unity, though actual values between 0.3 and 1.3 have been suggested in the literature. The results reported in the present paper have been obtained using $Sc_t = 0.7$. Because the closure coefficient for the subgrid stresses is a dynamic variable within the present formulation, the turbulent diffusivity is also a dynamic function of the local flow properties. The turbulent Prandtl number, evaluated dynamically as presented in the previous section, was found to vary in the mixing regions between approximately 0.4 and 0.9 as shown later for the reacting flow, corresponding to a turbulent Lewis number varying between 0.7 and 1.4. Rather than fixing the turbulent Schmidt number to a constant, another modeling approach could have been to fix the Lewis number to unity and let the turbulent Schmidt number vary with the dynamic evaluation of Pr_t. This method was, however, not tested. It should be also noted that no significant differences were found in the preliminary results of the reacting flowfield when decreasing the closure coefficient to $Sc_t = 0.4$. Nevertheless, a dynamic evaluation of Sc_t or a more comprehensive subgrid mixing and reaction model based on an LES with linear-eddy mixing (LEMLES) [35–37] approach could be used, and will be considered in a future study.

3. *Realizability Conditions for the Subgrid Stress Model*

The realizability conditions [6] are usually satisfied by the LDKM formulation for the computation of well-resolved and fully turbulent simulations [38]. Nevertheless, an explicit enforcement of the realizability constraints is performed in this study. The realizability constraint is given by

$$\begin{cases} |\tau_{12}^{\text{sgs}}|^2 \le \tau_{11}^{\text{sgs}} \tau_{22}^{\text{sgs}} \\ |\tau_{23}^{\text{sgs}}|^2 \le \tau_{22}^{\text{sgs}} \tau_{33}^{\text{sgs}} \\ |\tau_{13}^{\text{sgs}}|^2 \le \tau_{11}^{\text{sgs}} \tau_{33}^{\text{sgs}} \end{cases} \tag{24}$$

With the closure adopted in the present study, these three relations are rearranged to show that the following inequality should always hold:

$$c_v \le \frac{\sqrt{k^{\text{sgs}}}}{\sqrt{3} \tilde{S} \bar{\Delta}} \tag{25}$$

where

$$\tilde{S}^2 = \frac{1}{2} \left(\tilde{S}_{ij} - \frac{1}{3} \tilde{S}_{kk} \delta_{ij} \right) \left(\tilde{S}_{ij} - \frac{1}{3} \tilde{S}_{kk} \delta_{ij} \right) \tag{26}$$

C. Computational Method

A finite-volume methodology is used to solve the governing equations for LES of compressible flows described in the previous section. A predictor/corrector time-integration methodology is used here, resulting in a second-order time-accurate computation. Advancement from the iteration n to iteration $n + 1$ is performed according to the following two-stage method:

$$\begin{aligned} Q^{(\star)} &= Q^{(n)} + dQ^{(n)} \qquad \text{(Predictor)} \\ Q^{(n+1)} &= \frac{1}{2}[Q^{(n)} + Q^{(\star)} + dQ^{(\star)}] \qquad \text{(Corrector)} \end{aligned} \tag{27}$$

where $dQ^{(n)}$ and $dQ^{(\star)}$ are obtained from the fluxes evaluated based on $Q^{(n)}$ and $Q^{(\star)}$, respectively.

The interface fluxes are evaluated using a hybrid methodology developed for the resolution of turbulent fields in supersonic, and potentially shock-containing environments. Hybrid schemes have the potential to capture shocks locally while resolving the turbulent features of the flow with minimal dissipation, and have been the focus of many recent scheme developments [7,8,39]. The fluxes computation is hereafter presented for the $(i + 1/2, j, k)$ interface only, for brevity. The flux evaluation is given by

$$F_{i+1/2} = \lambda_{i+1/2} F^s_{i+1/2} + (1 - \lambda_{i+1/2}) F^u_{i+1/2} \tag{28}$$

where F^s is the flux obtained using a low-dissipation scheme adapted to the resolution of turbulent flows, whereas F^u is evaluated using an upwind scheme, adapted to the capture of flow discontinuities. The current hybrid methodology uses a Heaviside step function to switch between numerical schemes

$$\lambda_{i+1/2} = \begin{cases} 1 & \text{if } \max(S_{P,i}, S_{P,i+1}, S_{\rho,i}, S_{\rho,i+1}) \le 0 \\ 0 & \text{otherwise} \end{cases} \tag{29}$$

S_P and S_ρ are smoothness parameters formulated based on the curvature of the pressure field and of the density field, respectively. The formulation of the smoothness parameter for variable ϕ ($\phi = P$ or $\phi = \rho$) is given by

$$S_{\phi,i} = \begin{cases} \frac{|\phi_{i+1} - 2\phi_i + \phi_{i-1}|}{|\phi_{i+1} - \phi_i| + |\phi_i - \phi_{i-1}|} - S_\phi^{\text{th}} & \text{if } |\phi_{i+1} - 2\phi_i + \phi_{i-1}| \ge \epsilon_\phi \phi_i \\ -S_\phi^{\text{th}} & \text{otherwise} \end{cases} \tag{30}$$

The coefficients ϵ_P and ϵ_ρ are taken to be equal to 0.05 and 0.1, respectively. The threshold values for the pressure and density switches S_P^{th} and S_ρ^{th} are equal to 0.5 and 0.25, respectively. These coefficients were found from numerical experimentations to yield accurate simulations of turbulent flows in the presence of shocks (shock/turbulence and shock/shear interactions) and/or density interfaces (Richtmyer–Meshkov Instabilities [40]).

The resolution of turbulent structures away from the discontinuities is based on a low-dissipation flux evaluation F^s obtained using a central scheme formulation. This method is an extension of the original McCormack scheme [41], and alternates upwind and downwind flux evaluations over the predictor/corrector time sequence. This procedure allows a reduction of the truncation error and results in a formally central scheme but ensures stability due to its inherent built-in dissipation. The present formulation extends the original formulation to reach fourth-order spatial accuracy [38], and has been successfully applied to a wide variety of flows in studies of subsonic turbulent flows [42], high-speed turbulent, albeit shock-free, mixing flows [23,43], as well as for the studies of flame-turbulence interaction [44] or gas turbines [45].

F^u is obtained using a shock-capturing scheme. The upwind method uses a MUSCL-type interpolation (monotone upstream centered schemes for conservation laws, [46]) for the reconstruction of the Riemann problem at the cell interface. A monotonized central limiter is used for this operation to ensure total variation diminishing property, and the interpolation is applied to the primitive variables. Furthermore, the flattening method described by Colella and Woodward [47] in the development of the Piecewise Parabolic Method scheme is used to prevent steep and strong shocks from creating unphysical oscillations in postshock regions.

A hybrid Riemann solver is employed in the present study to reduce the sensitivity to the odd–even and carbuncle instabilities [48]. The modified Harten–Lax–van Leer (HLL) [49] approximate Riemann solver of Toro et al. [50] (HLLC) is used as a default solver to obtain the interface fluxes from the reconstructed states. This solver yields a robust and yet accurate resolution of hydrodynamics problems. Fluxes evaluations revert to the two-waves HLLE approximate solver [51] within shock thicknesses, in the directions transverse to the main front. This hybrid solver (HLLC/E) retains the accuracy of the base HLLC solver almost everywhere. This method shows very little sensitivity to the odd–even decoupling and to the carbuncle instabilities. The classical hypersonic bluff-body, kinked Mach stem, and shock propagation on a perturbed grid [48] test cases have been performed, and showed that the hybrid solver is only marginally unstable, compared with the HLLC or the Roe-solver. The wave-speed evaluations for the Riemann solver follow the method given in Einfeldt [51], based on the left-, right-, and Roe-averaged characteristic speeds.

The upwind scheme is used to resolve the shock waves and/or the density fronts in the direction of the wave propagation, lowering the order of accuracy within these regions. Typically, two to four grid cells are needed to resolve shock waves and contact discontinuities in the flow. The resolution of the convective and the pressure forces is fourth-order accurate away from the discontinuities. The evaluation of the viscous fluxes is performed using a standard finite difference at the cell interfaces, resulting also in a fourth-order accurate method.

The parallelization capability of the numerical method is an important aspect of this development due to the relatively high computational time required for a practical Scramjet simulation. The reacting case presented here required over 13,000 single CPU hours of computation to collect statistical data, that is, excluding the computational time required to ignite the mixture, stabilize the simulation, and get statistically stationary results. The numerical methodology presented above has been integrated in a parallel solver. Communication is implemented using a standardized message-passing interface (MPI) protocol. The resulting numerical code is portable and has been used on multiple platforms with different architectures (Intel PC linux cluster, Cray XT4, IBM SP4 clusters, etc.). The performance of the implementation on parallel clusters depends on the domain decomposition and the amount of switching between numerical schemes inside a given domain, but the implementation of both the upwind and central schemes independently has been found to scale well, almost linearly, for up to 1024 processors on multiple architectures [52].

D. Verification of the Large-Eddy Simulation Approach in Supersonic Turbulent Flows

The LES method used in the present study has been developed to permit the proper resolution of turbulent flows in supersonic environments, by limiting the use of a shock-capturing scheme to the discontinuous regions of the flow. The validity of this methodology is illustrated here in a study of shock/isotropic turbulence interaction problem similar to case B of Lee et al [53]. A field of isotropic turbulence is generated in a domain of dimensions $6\pi \times 2\pi \times 2\pi$, such that the Taylor microscale Reynolds number $R_\lambda = 20$ and the turbulent Mach number $M_t = 0.11$. The initial energy spectrum is given by:

$$E(k) = 16\sqrt{\frac{2}{\pi}}\frac{u_{\text{rms}}^2}{k_0}\left(\frac{k}{k_0}\right)^4 \exp\left[-2\left(\frac{k}{k_0}\right)^2\right] \tag{31}$$

where $k_0 = 4$ is the most energetic wavelength of this initial spectrum.

This field of isotropic turbulence is used at the inflow of a spatial problem of dimensions $(2\pi + 1 \times 2\pi \times 2\pi$. A $M = 2.0$ standing shock is initialized at $x = \pi$ from the Rankine-Hugoniot relations

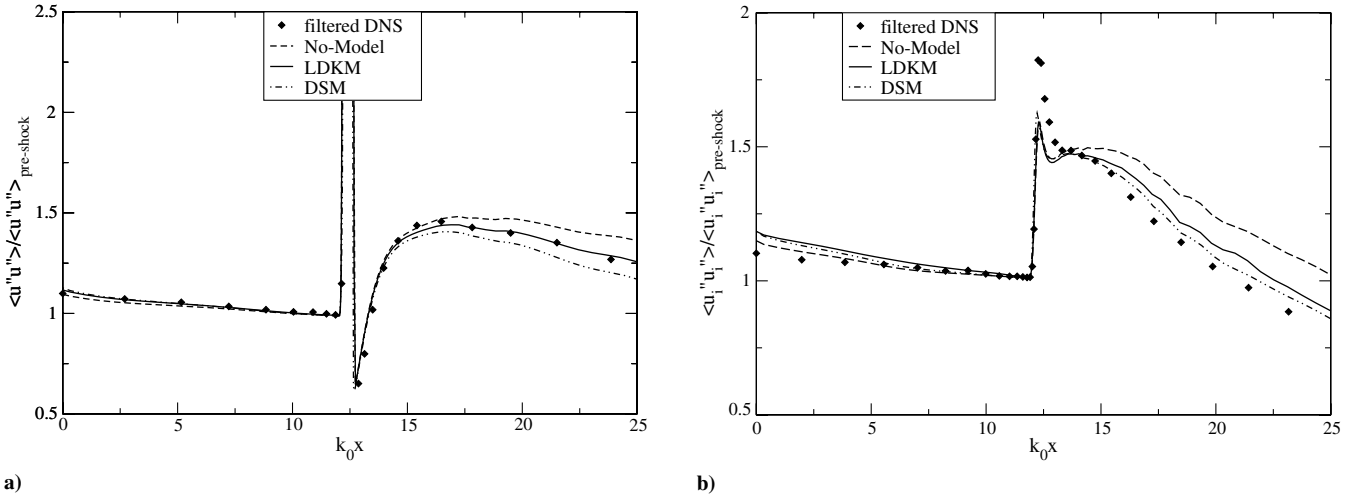

a) b)

Fig. 1 Profiles of axial Reynolds stresses for the shock/turbulence interaction. Comparison between LES and filtered DNS results.

based on the mean incoming thermodynamics state. A direct simulation of the configuration has been performed, showing a good capture of the physical phenomena involved in the interaction, and comparing well to the reference data of Lee et al. [53]. The DNS field is filtered and used to initialize the LES simulation, performed on a $106 \times 32 \times 32$ cells grid. Figure 1a represents the statistical averages of the Reynolds stresses in the shock-normal direction using the current hybrid method, along with the LDKM model described above, the results obtained using the Dynamic Smagorinsky Model (DSM) [34], and a simulation without closure model, along with the results from the filtered DNS fields. The present LES methodology captures the shock locally, and permits a proper resolution of the turbulence amplification. The peak in fluctuations of axial velocity and the decay rate further downstream are correctly simulated with the LDKM closure model. The location of the peak in transverse velocity fluctuations downstream of the interaction occurs some short distance downstream of the DNS predictions, but the subsequent turbulent decay is captured at the right rate. This prediction of the transverse velocity has also been observed in other LES studies [54]. Overall, the present LES strategy is found to capture the fundamental problem of shock/turbulence interaction with good accuracy. The use of the upwind numerical scheme remains limited in space to a region near the shock front, and the resolution of the turbulent field is ensured by the low-dissipation scheme, which permits a good capture of the spectral behaviors of the turbulent fields in the pre and postshock regions (not shown here for brevity), over a relatively coarse grid resolution. This LES methodology can now be applied to a configuration of practical interest.

III. Strut-Based Scramjet

A. Computational Configuration

The LES method described above is applied to the study of a generic Scramjet test rig. A schematic of the chamber is given in Fig. 2. Vitiated air (23.2% O_2, 73.6% N_2, 3.2% H_2O in mass) enters a 50 mm $\times$ 40 mm cross-section combustion chamber at $M = 2$. From $x = -9$ mm on, the upper wall of the test chamber diverges with a constant angle of 3 deg to compensate for the boundary-layer growth. A wedge is placed at the centerline, $y = 25$ mm, in the chamber. The wedge is 32 mm long and its half-angle is 6 deg. The base of the wedge is placed at $x = 0$. Hydrogen is injected at the center of the base of the wedge through 15 holes of diameter 1 mm and 1.4 mm apart. Following the work of Oevermann [16], the freestream velocity is fixed to 732 m/s, for a static pressure of 100 kPa and a static temperature of 340 K. The ports for the hydrogen injection system are choked, the fuel is assumed to have a velocity of 1200 m/s, and static pressure and temperature at the exit plane are 100 kPa and 250 K, respectively. The stagnation enthalpy of this experimental facility is rather low compared with a practical Scramjet engine flight enthalpy, but this configuration remains challenging to simulate and allows for interesting flow physics to be captured.

For the simulation of nonreacting flow presented here, two injection holes have been simulated and periodic boundary conditions have been applied in the transverse direction. The inflow being a $M = 2$ supersonic flow, characteristics cannot propagate upstream of the flow, and the boundary is fully imposed based on the static conditions previously given. Similarly, given that the Mach number of the hydrogen jets is unity, the boundary conditions for the jets' inflow were fully imposed. At the domain outlet the flows for both nonreacting and reacting simulations are supersonic, and these boundaries are thus treated using extrapolations from the interior of the domain. The upper and lower walls are assumed to be slip boundary conditions to avoid resolving the wall boundary layers. The computational resolution of shock/boundary layer interactions in moderate Reynolds number flows is an ongoing topic of study [55], and requires several million grid cells to resolve properly. The resolution of the shock/boundary layer interactions that occur in the present high Reynolds number flow along these upper and lower walls would require an extremely fine resolution, resulting in a prohibitive computational cost, and is out of the scope of this study. This approximation is also considered acceptable for now because the focus here is on the mixing and reaction that occur some short distance downstream of the injector in the wake of the wedge. The physics involved in the mixing/reaction in the near field is relatively independent of the top and bottom wall behavior, which only influences the mixing/reaction zones at some distance $x \geq 100$ mm. The surfaces along the wedge are, however, simulated as no-slip walls. Furthermore, the approximation of slip conditions at the top and bottom walls permits an increase in refinement along the walls of the wedge and in the shear layers. All walls are treated using adiabatic conditions. Given the rather low streams temperatures and the fact that the zones of combustion in the reacting case are far from the walls, the heat exchange between the rig surfaces and the streams is expected to be small, and not to change the flow evolution significantly. Furthermore, to the knowledge of the authors, thermal exchanges have not been measured during the experimental campaign. The cold flow was initialized using the conditions at the main inflow throughout the domain, except in the wake of the wedge where the static pressure and temperature remained unchanged, but the velocity was set to zero. The simulation was then conducted until stationary state was achieved and statistics could then be collected. The initialization of the reacting flow simulation was performed from a realization of the stationary cold flow simulation, and will be described in more detail in Sec. III.C.

A multiblock decomposition is used during these simulations, with two blocks located on the lower and upper side of the wedge at $x \leq 0$ and have been discretized with $109 \times 56 \times 50$ and $109 \times 58 \times 50$ grid cells, respectively. The third block is located downstream of the wedge $x \geq 0$ and is resolved using $211 \times 180 \times 50$ grid cells. The resolution was refined along the walls of the wedge at the jets' inflow locations, and along the developing shear layers. This grid resolution is similar to other past studies of Scramjet flowfields in similar configurations [18,56], and allows over 15 points in the initial stage of each shear layer, considered reasonable based on past

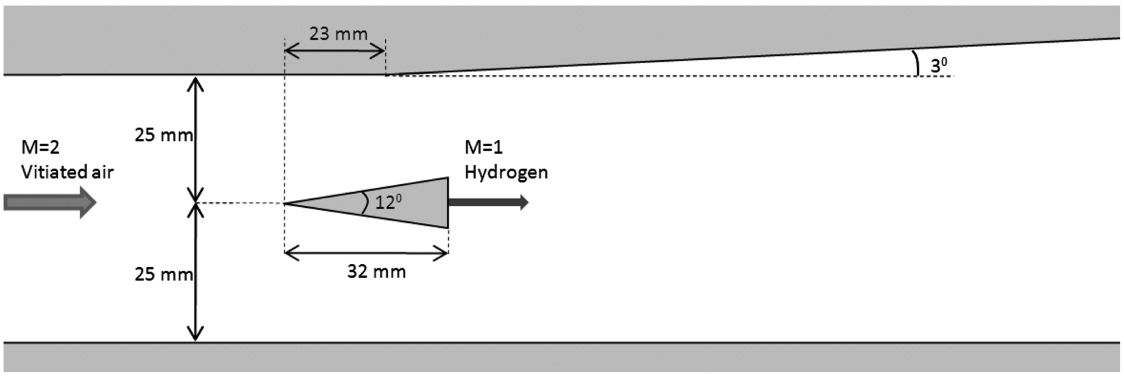

Fig. 2 Schematic of the Scramjet combustion chamber.

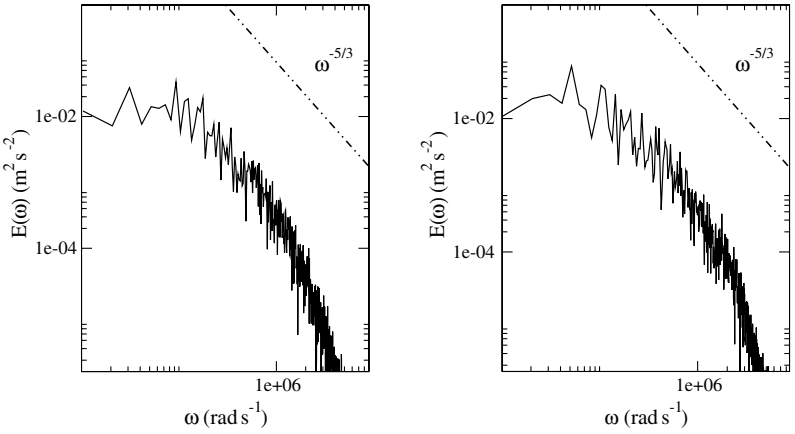

a) $x = 3$ *mm*, $y = 28$ mm **b) $x = 9$ *mm*, $y = 26.5$ mm**

Fig. 3 Spectra of kinetic energy at two locations within the shear layer at two locations: $x = 3$ mm, $y = 28$ mm and $x = 9$ mm, $y = 26.5$ mm.

studies of high-speed shear layers [38,43] or compared with other studies of similar configurations [18]. The spectra of turbulent kinetic energy, collected in the shear layers and represented in Fig. 3, recover the $k^{-5/3}$ law indicating the appropriateness of the computational grid to the resolution of this turbulent problem. Effects of grid resolution were also addressed in past studies and are not revisited here. It should be noted, however, that the far-field (in the downstream direction) resolution is considered marginal but the focus of this study remains on the near-field features.

B. Nonreacting Flow

A Schlieren image of the experimental tests is shown in Fig. 4 along with the numerical contours of gradients of instantaneous and time-averaged density fields under similar operating conditions, highlighting the principal flow features of this configuration. Overall, the characteristic flow patterns obtained numerically show a fair agreement with the experimental observations. The supersonic incoming flow is deflected at the tip of the wedge, and two shocks are formed symmetrically on each side. These shocks will be denoted shock A (upper) and shock B (lower). After impacting the upper and lower walls, they reflect back toward the centerline of the test chamber. The impact of shock A on the upper wall occurs at $x = 1$ mm, downstream of the location of the top wall divergence. As a consequence, the oblique shock interacts with the upper wall expansion fan and the shocks' trajectories become asymmetric. After reflection, they intersect at $y = 29$ mm, well above the centerline of the chamber.

At the base of the wedge the boundary layers formed along the walls of the strut separate and, due to the low pressure in the recirculation region, form two symmetric shear layers that converge toward the centerline. The flow divergence leads to the formation of two expansion fans at both corners of the wedge. Again, due to the low pressure, the hydrogen jet is underexpanded and expands into a diamond-shaped structure. As the shear layers curve back and start mixing with the hydrogen jet, compression waves are generated on each side that soon turn into shock waves. The upper wave merges with the transmitted shock B before reaching the upper wall. From this interaction, a slip line is formed and propagates along the upper wall. On the lower side of the test chamber, the shear-layer-based compression interacts with the expansion fan and curves toward the lower wall. It merges with shock A after reflection on the bottom wall only. Finally, both reflected shocks intersect further downstream at $y = 27$ mm, closer to the centerline of the tunnel.

Despite many similarities, some differences are observed between experimental and numerical flowfields. First, because the upper and the lower wall boundary layers are not simulated, the influence of shock/boundary layer interactions is neglected here. It is seen from the experimental visualizations that these interactions have an impact on the reflection of shock B on the upper wall. The boundary-layer separation strengthens the incoming shock, and two shocks are issued after reflection. This feature will have an influence on the flow close to the centerline for $x \geq 100$ mm and is not modeled here. Second, two waves are seen in the Schlieren image that emerge from the edges of the wedge. These waves are slightly stronger than regular Mach waves and might impact the flowfield evolution. Their strength is, however, believed to be rather limited, as their angles remain close to 36 deg angle-of-Mach waves under these conditions. Finally, several low-intensity waves are observed in the experimental results, probably due to small imperfections in the tunnel surfaces, but their influence on the flow evolution should be rather small.

During the experimental campaign performed at DLR on the present Scramjet configuration, measurements of the velocity flowfield have been performed using particle image displacement velocimetry and laser Doppler velocimetry (LDV). The profiles of density-weighted averaged velocity obtained at six different axial locations, $x = 11$ mm, $x = 58$ mm, $x = 90$ mm, $x = 115$ mm, $x = 140$ mm, and $x = 166$ mm, are presented in Fig. 5 and compared with experimental profiles obtained with LDV measurements where available. The velocity profile at the first location differs from the experimental results in the core region. The extent of the recirculation

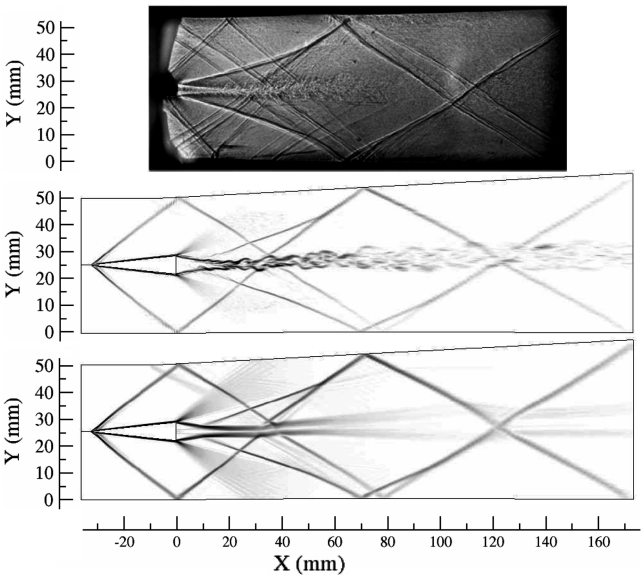

Fig. 4 Top: Experimental Schlieren image of the test chamber for the nonreacting flow. Middle: Instantaneous density gradient contours in the centerplane from the numerical simulation of nonreacting flow. Bottom: contours of time-averaged density gradient in the centerplane from the numerical simulation of nonreacting flow.

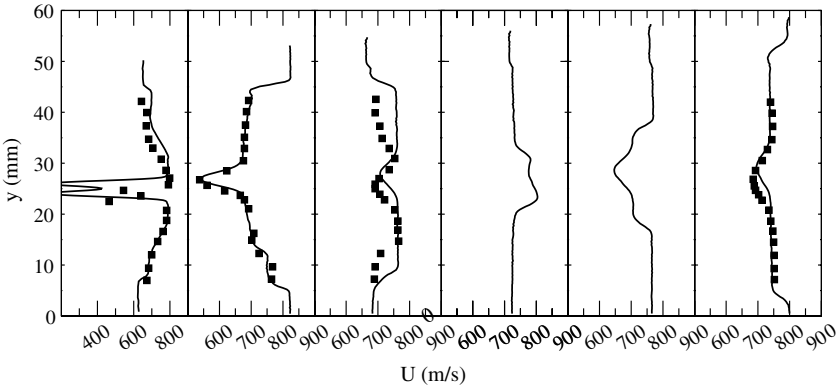

Fig. 5 Transverse profiles of mean axial velocity (lines) at $x = 11$ mm, $x = 58$ mm, $x = 90$ mm, $x = 115$ mm, $x = 140$ mm, and $x = 166$ mm for the nonreacting case, compared with available experimental data (symbols).

region is overpredicted in the numerical simulation, which shows a maximum velocity of 400 m/s in the wake of the jet, whereas the experiments show a peak velocity at the centerline of around 700 m/s. Similar predictions were obtained in the LES study of Berglund and Fureby [18]. Further downstream, a good agreement in axial velocity magnitudes is achieved. The vertical location of peak velocity is not necessarily in agreement. It should also be noted that the double shock generated from the upper shock/boundary-layer interaction reported earlier has a clear impact on the upper portion of the velocity profile at the location $x = 90$ mm, which shows a velocity defect due to the transverse wave.

The profiles of static pressure along the bottom wall of the experimental and numerical studies are represented in Fig. 6. The initial decrease in pressure is associated with the impact of the expansion fan generated at the lower corner of the wedge with the wall. As the primary shock (formed by the curving of the shear layer) and the transmitted shock A impact the lower wall, the pressure rises. Consistent with the observations in Fig. 4, the numerical resolution shows two separate peaks in pressure. The experimental results show one peak only, and further upstream. The differences observed are probably due to the location of the shear layer recompression that is slightly downstream in the simulation and to the separated wall

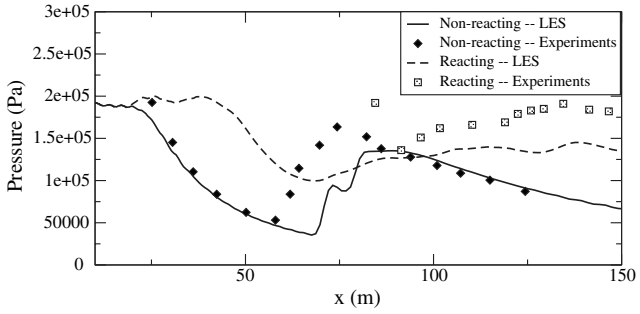

Fig. 6 Axial profiles of static pressure along the bottom wall (solid line: nonreacting, dashed line: reacting), compared with available experimental data (diamond symbols: nonreacting, square symbols: reacting).

boundary layer in the experiments, as a consequence of the shock/boundary-layer interaction, neglected in the present computation. It is noted that these results are in qualitative agreement with other reported studies [16,18] of this configuration.

The time-averaged flow features show a reasonable agreement with the experimental results, but do not highlight the unsteady nature of the flowfield. The instantaneous contours of density gradient, shown in Fig. 4, highlight some of the dynamics of the unsteady flow. Although the shocks pattern is found to be rather steady and insensitive to the dynamics of the recirculation region and of the shear layers, the wake of the bluff body is highly unsteady. The recirculation region is confined between the high-speed underexpanded jet and the freestream shear layers, and is subject to high levels of shear and to the formation of vortical structures, as illustrated in Fig. 7a. These unsteady vortical structures contribute to the mixing of the hydrogen jet with the recirculation fluid. The hydrogen jet penetrates deeply into the recirculation region. As the jet interacts with the converging shear layers it breaks down and localized vortices are formed. In the early stage of the shear layers development Kelvin–Helmholtz instabilities are generated, which leads to the formation of two-dimensional, spanwise vortices. However, the shear layers are at the interface between the high-momentum freestream fluid and the highly unsteady recirculation region and show three-dimensional structures, as shown in Fig. 7b, where an isosurface of density shows the corrugation of the shear layers and the formation of vortical structures that increase the mass exchange between the freestream and the recirculation region. Further downstream as the shear layers interact with the hydrogen jet, the wake flow shows an unstable behavior, a combination of Kelvin–Helmholtz instabilities and von–Karman vortex street. Here again, two-dimensional, spanwise vortices are created and lead to an ondulatory evolution of the wake. Furthermore, the interaction of the reflected shocks A and B with the wake increases the level of vorticity, the growth rate of the wake is enhanced, and the levels of turbulence amplified.

Figure 8 shows the profiles of turbulent fluctuating velocities at the same six locations as stated previously. Again, comparison with experimental data is made where available. High-intensity velocity

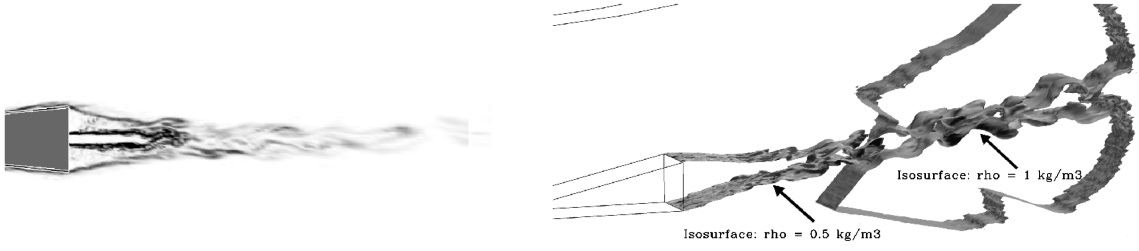

a) Vorticity magnitude **b) Iso-surfaces of density**

Fig. 7 Instantaneous fields for the nonreacting flow: a) contours of vorticity magnitude close to the injection region (-10 mm $< x < 65$ mm, 13 mm $< y < 37$ mm, and b) isosurfaces of density.

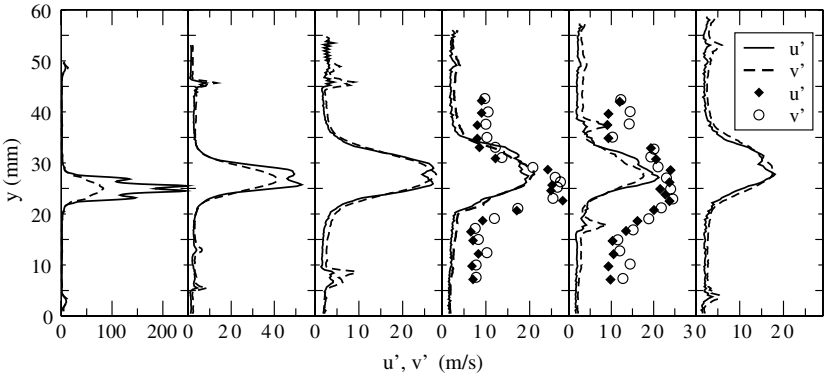

Fig. 8 Transverse profiles of fluctuating velocities (lines) at $x = 11$ mm, $x = 58$ mm, $x = 90$ mm, $x = 115$ mm, $x = 140$ mm, and $x = 166$ mm for the nonreacting case, compared with available experimental data (symbols).

fluctuations are found along the boundaries of the jet. This effect is amplified as the shear layers converge and merge with the jet. The peak fluctuations are obtained at the first location of data collection. The very high velocity of the jet penetrating into the low-velocity recirculation zone leads to a significant level of turbulent production, and rather high values of the turbulent Mach number $M_t \approx 0.3$ and the dynamic evaluation of c_v leads to increasing values of the Reynolds stresses close to the jets. Consequently, further downstream the turbulent fluctuations decay progressively. The comparison with experimental data shows a reasonable capture of the turbulent intensity, though the extent of the turbulent region is not fully recovered. Here again, these locations are downstream of the interaction between the wake and the double shock. The small peaks in turbulent fluctuations away from the wake, observed in Fig. 8 (e.g., at $y =$ 8 mm in the third plot) are related to the small unsteadiness of the shock waves. The shocks oscillations are due to the shock fronts' corrugation as a consequence of their interaction with the large-scale vortices generated within the wake and along the shear layers. These oscillations generate velocity fluctuations similar to the shock/turbulence interaction considered earlier in Sec. II.D.

C. Reacting Flow

The formation of recirculation regions is a fundamental aspect and a requirement for an efficient flame-holding in a supersonic combustion chamber. Such features permit to trap hot products, and can initiate and anchor the flame. In the case of wedge injection in a supersonic flow, the dead zone at the base of the body seems ideally suited to the purpose of flame anchoring. The actual flame stabilization mechanism for this scramjet configuration is now examined.

The strut-based scramjet configuration considered earlier in nonreacting flow has also been studied for reacting flow under the same operating conditions, at DLR [13–15] and numerically [16–20]. From a numerical point of view, the use of detailed reaction mechanisms is computationally expensive, and it is generally standard to employ simplified, reduced mechanisms to simulate combustion processes in scramjet engines. The choice of the simplified reaction mechanism is, however, an important factor for the relevance of the results. Berglund and Fureby [18] suspected the simplified two-step reaction mechanism of Rogers and Chinitz [57], used in their ([18]) and other ([17]) studies, to result in an improper capture of the reaction rates and to underestimate the flow expansion behind the strut. Later, Berglund et al. [56] showed that a seven-step reaction mechanism for H_2/O_2 combustion similar to the mechanism adopted here compared well to a more detailed nineteen-step reaction model [58] in terms of induction time, and performed better than other simplified one- or two-step mechanisms for the simulation of a wedge-based scramjet engine, though not exactly the same as the configuration considered here. In the present study, a modified version of the Spark model employed by Eklund et al. [59], and more recently by Baurle and Girimaji [60] for the study of high-speed hydrogen combustion, is employed. The forward rates are given by

$$
\begin{aligned}
&\mathrm{H_2 + O_2 \rightarrow OH + OH} && k_1 = 1.70 \times 10^{13} e^{-24157/T} \\
&\mathrm{O_2 + H \rightarrow OH + O} && k_2 = 1.20 \times 10^{17} T^{-0.91} e^{-8310.5/T} \\
&\mathrm{H_2 + OH \rightarrow H_2O + H} && k_3 = 2.20 \times 10^{13} e^{-2591.8/T} \\
&\mathrm{H_2 + O \rightarrow OH + H} && k_4 = 5.06 \times 10^{4} T^{2.67} e^{-3165.6/T} \\
&\mathrm{OH + OH \rightarrow H_2O + O} && k_5 = 6.30 \times 10^{12} e^{-548.6/T} \\
&\mathrm{OH + H + M \rightarrow H_2O + M} && k_6 = 2.21 \times 10^{22} T^{-2} \\
&\mathrm{H + H + M \rightarrow H_2 + M} && k_7 = 7.30 \times 10^{17} T^{-1}
\end{aligned} \tag{32}
$$

and the backward reaction rates are found using thermodynamic equilibrium constants for each reaction. The chaperon efficiencies for the two last reactions are given by H_2:2.5, H_2O:16, and 1 for all other species. Following the explicit formulation of the numerical method, and given the grid resolution in the mixing and reacting regions of the order of 200 μm, the computational timestep imposed by the Courant–Friedrichs–Lewy condition is comparable to the characteristic chemical time of the initiation reaction. Euler time-integration of the chemical source terms using 20 subiterations is performed, rather than solving exactly the system of differential equations. This approach has been shown [61] to permit a proper capture of the critical reactions, and the stiffest steps are assumed to be in quasi equilibrium. The combustion regime was found during the experimental study of this scramjet configuration [14,15] to lie between corrugated flamelets and distributed reaction zone, and hence, the reaction zone is subject to high levels of turbulent stirring. With the present grid refinement at the base of the wedge, the smallest eddies at the resolved scale are of sizes comparable to the flame thickness. Comparisons between mixing time scale at the subgrid level and chemical time scale show that, in the context of an Eddy Dissipation Concept closure, the reaction rate of the initiation evaluated using the Arrhenius laws based on the volume-averaged concentrations and temperatures dominate. As a first approximation, the latter approach is used to evaluate the reaction rates throughout this study. Here again, a more advanced reaction modeling based on the LEMLES [35–37] approach could be used, and will be considered in a future study.

The ignition of a reactive mixture is a challenging task for both experimental and numerical studies of reacting flows. This is particularly true in the configuration of interest here, given the low temperatures of the incoming streams of oxidizer and fuel and the rather small equivalence ratio ER ≈ 0.035. In the present study, the simulation of reacting flow was restarted from a fully developed flowfield of the cold flow simulation, and ignition was achieved by creating a region of hot reactant mixture in the wake of the wedge, and by simultaneously increasing the Arrhenius coefficients of the reaction mechanism employed by adjusting the temperature dependence in the exponential terms of the Arrhenius coefficients to a minimum of 1300 K, hence enhancing reaction in the cold regions. This numerical trick permitted a fast transition to reacting flow, and once stable combustion was achieved the reaction rates were

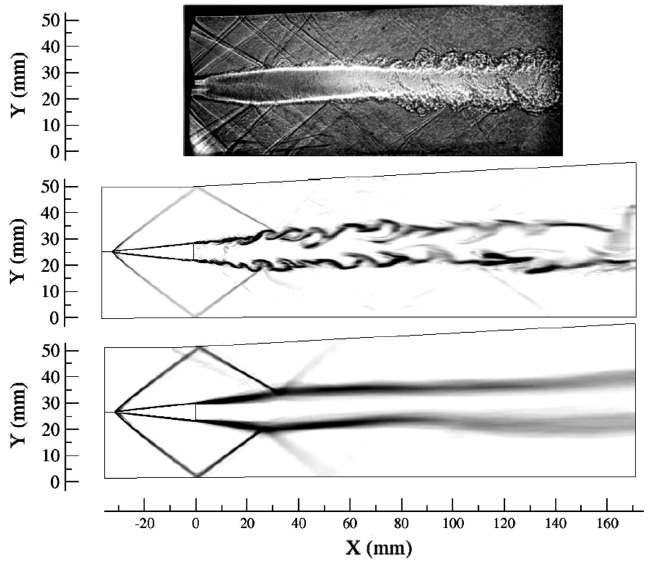

Fig. 9 Top: Experimental Schlieren image of the test chamber for the reacting flow. Middle: Instantaneous density gradient contours in the centerplane from the numerical simulation of nonreacting flow. Bottom: contours of time-averaged density gradient in the centerplane from the numerical simulation of nonreacting flow.

progressively decreased back to their nominal values, and the simulation was conducted until stationary conditions within the actual simulation parameters were achieved. Because no specific coupling between the two jets simulated in the nonreacting flow was observed numerically, the computational domain was reduced to simulate only one injector for computational savings.

The experimental Schlieren and numerical density gradient contours are shown in Fig. 9 for the reacting case. The pressure at the base of the wedge increases as the reaction is initiated. As a consequence, the shear layers do not converge toward the centerline, but rather expand at an angle slightly greater than the wedge walls, and two weak shocks are formed at each corner. As shocks A and B interact with the wake shear layer they reflect as weak expansion waves, and the shear layers that delimit the wake region bend back to (close to) horizontal. As a consequence, the flows in the wake and in the freestream are quasi parallel with equal pressure, and only small waves are observed further downstream. The experimental and numerical pressure profiles along the lower wall are represented in Fig. 6 along with the nonreacting case. The pressure is found to increase slightly at $x \approx 25$ mm where, in the nonreacting simulation, the pressure started decreasing. This is in accordance with the behavior of the shear layers at the corner of the wedge, which expand slightly compared with the angle of the side walls of the wedge. The weak shocks formed due to this area restriction propagate at a direction close to Mach waves, and induce an increase in pressure. As the shear layers swerve back in the direction of the mean flow, expansion fans are formed and lead to a decrease in static pressure at the wall, starting at $x \approx 45$ mm. Further downstream, as the flow is mostly parallel, only small changes are observed in the pressure profile.

The velocity profiles shown in Fig. 10 show the strong expansion of the wake of the wedge. A velocity defect is observed at the first station, which corresponds to the formation of two recirculation regions on each side of the jet. The strength of these recirculations is predicted higher in the numerical resolution, which captures a localized reverse flow not seen in experiments. Further downstream the wake region expands and stabilizes to a fixed width, in good agreement with the experimental observations.

Another consequence of the pressure rise at the base of the wedge is a lower penetration of the jet into the recirculation region. The mixing region in the time-averaged field is shown in Fig. 11. The jet has a rather low penetration, and two vortices on each side of the jet enhance the level of mixing of the hydrogen with the recirculation fluid. Further downstream the reaction and volumetric expansion create a bubble of hot products, and the circulation imposed by the outer flow creates a reverse flow along the centerline toward the injection, hence initiating the flame.

The profiles of averaged temperature at the six collection locations are shown in Fig. 12, and compared with the experimental profiles obtained from Coherent anti-Stokes Raman spectroscopy . The temperatures predicted at the first location slightly underestimate the values measured experimentally, and show some asymmetry not observed in the experiments. The values of peak temperature are in better agreement further downstream. The region of hot products is, however, slightly larger than in the experimental measurements. Despite a low equivalence ratio ER ≈ 0.035, the hydrogen is not entirely consumed before reaching the outflow of the domain. Yet most of the heat release occurs within the shear layer along the edges of the recirculation bubble, rather close to the injector. As the flow evolves downstream, little reaction occurs and the temperature distribution diffuses and flattens, as already seen in Fig. 12. This diffusion process is enhanced by the large-scale vortical motions formed along the shear layers of the wake.

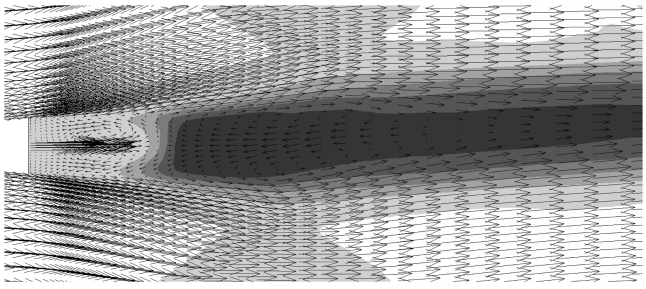

Fig. 11 Contours of the time-averaged static temperature field and velocity vectors in the injection and recirculation regions.

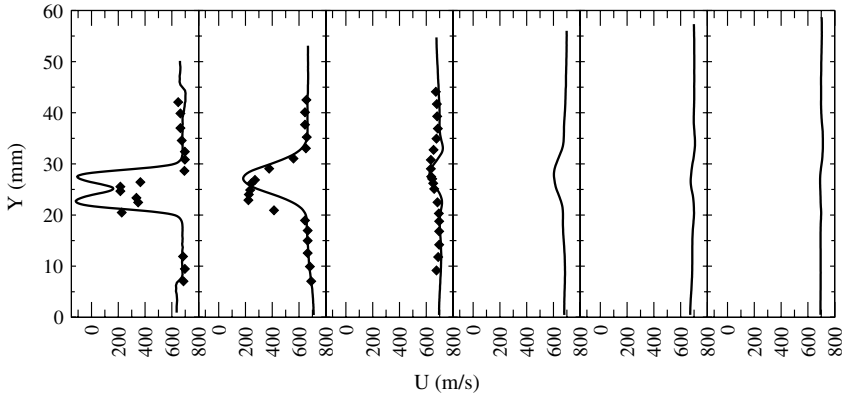

Fig. 10 Transverse profiles of mean axial velocity (lines) at $x = 11$ mm, $x = 58$ mm, $x = 90$ mm, $x = 115$ mm, $x = 140$ mm, and $x = 166$ mm for the reacting case, compared with available experimental data (symbols).

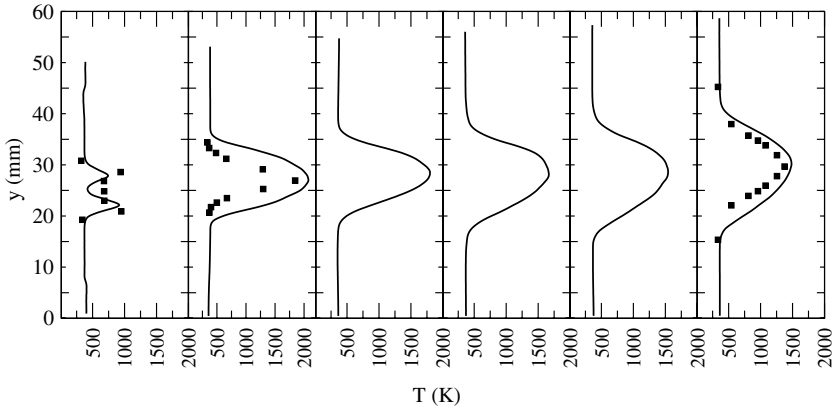

Fig. 12 Transverse profiles of time-averaged temperature (lines) at $x = 11$ mm, $x = 58$ mm, $x = 90$ mm, $x = 115$ mm, $x = 140$ mm, and $x = 166$ mm for the reacting case, compared with available experimental data (symbols).

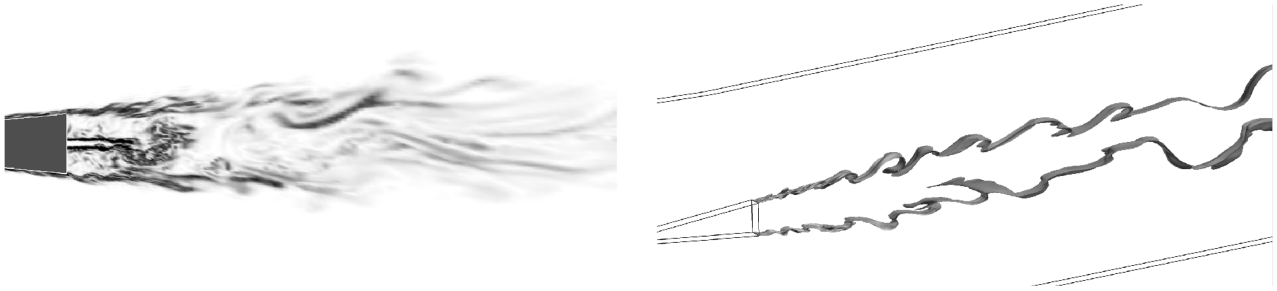

a) Vorticity magnitude **b) Iso-surfaces of density**

Fig. 13 Instantaneous fields for the reacting flow: a) contours of vorticity magnitude close to the injection region (-10 mm $< x < 65$ mm, 13 mm $< y < 37$ mm, and b) isosurfaces of density.

Similar to the cold flow simulation, the reacting flow evolution shows high levels of dynamics. In Fig. 13a, the contours of vorticity magnitude highlight the formation of flow instabilities within the recirculation region and the high level of dynamics. The jet penetration is reduced compared with the nonreacting case, and the jet breakdown is confined by the large recirculation bubble. Furthermore, the instabilities of the shear layer formed at the corners of the wedge can be identified. In the reacting flowfield, the shear layers do not converge toward the centerline and show a strong interaction with the low-velocity regions at the base of the wedge and in the recirculation bubble. As a consequence, Kelvin–Helmholtz instabilities develop along each shear layer, as seen in Fig. 13b, where an isosurface of density is represented for a given instant. Despite the three-dimensional nature of the flowfield in general, the large-scale vortices are two-dimensional and extend all along the spanwise direction of the wake. Similar vortical structures have been reported from planar laser induced fluorescence imaging of the reaction zone [14], though not for the same equivalence ratio. These structures play a fundamental role in the combustion process, as they generate a large-scale mixing of the freestream and partially reacted flow, bringing fresh gases into the recirculation regions (see Fig. 14). Downstream of the large recirculation region, an oscillatory motion of the wake is observed as the rather large vortices interact with the wake. Here again, this vortex street shows a mostly two-dimensional structure.

The recirculation regions formed along the jet boundaries do not carry hot products that initiate the flame continuously as expected from the cold flow and from the geometry design [13]. As observed earlier, hot products are trapped downstream of the injection. Intermittent reverse flows convect pockets of high-temperature fluid toward the injector. The temperature contours in Fig. 14 illustrate this phenomenon. Backflows on the lower and upper sides of the wake convect some of the hot products along the jet, and preheat the hydrogen and oxygen in this region.

The premixedness factor, defined as [62]

$$\alpha = \arccos\left(\frac{\nabla Y_{\mathrm{H}_2} \cdot \nabla Y_{\mathrm{O}_2}}{\|\nabla Y_{\mathrm{H}_2}\| \times \|\nabla Y_{\mathrm{O}_2}\|}\right) \tag{33}$$

is used to analyze the flame structure. Lower values of α are representative of a premixed system, whereas high values ($\alpha \approx 180°$) are characteristic of nonpremixed behavior. The premixedness index of two instantaneous flowfields is shown in Fig. 15. To make these contours relevant, the contours are shown for regions of positive production rates of H_2O only. The strong dynamics of the flame are highlighted in these results. The base of the wedge is a region where

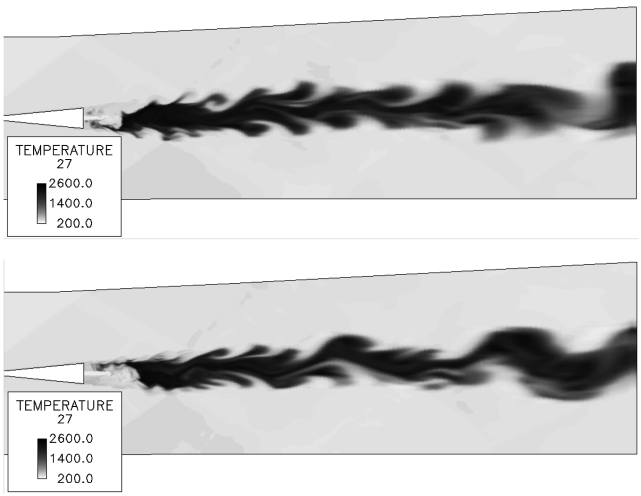

Fig. 14 Contours of the instantaneous static temperature fields for two instants 35 μs apart.

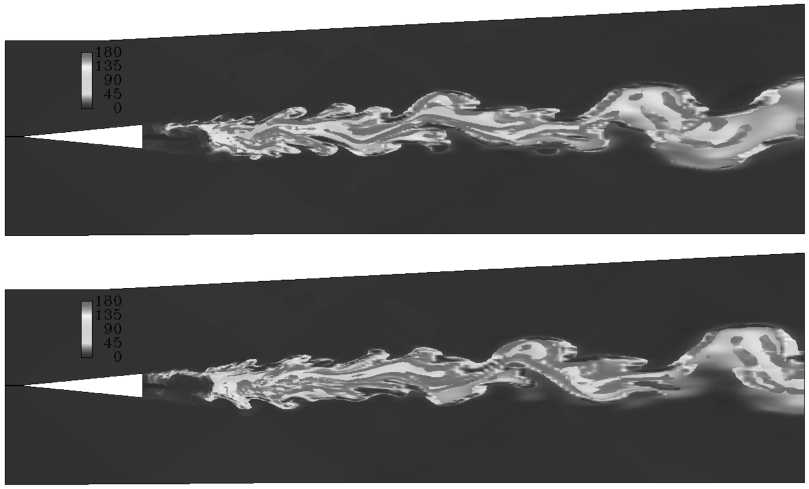

Fig. 15 Contours of the instantaneous premixedness index for two instants 35 μs apart. Background field is the temperature.

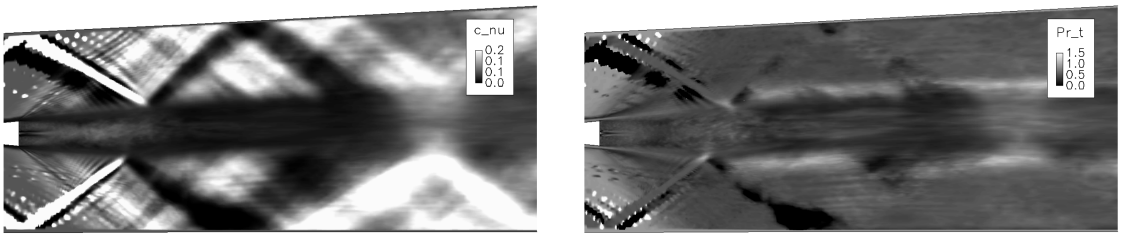

a) Contours of c_v **b) Contours of Pr_t**

Fig. 16 Contours of time-averaged closure coefficient for the subgrid stresses, c_v, and for the subgrid diffusion of enthalpy Pr_t for the reacting flow.

mixing occurs between the injected hydrogen and the incoming air. As a consequence, the convection of hot products upstream of the large recirculation region induces ignition of a partially premixed system, as visible in the first instantaneous contours of α in Fig. 15. At some later time the hot region generated by the premixed combustion is the center of a diffusion flame, as illustrated in the second instantaneous contours of α in Fig. 15, but combustion in this region weakens and finally dies out.

Most of the reaction and heat release occur as the premixed fluid within the shear layer is convected along the recirculation region and ignited. Also, the large vortical structures identified earlier contribute to the fluid mixing and to the penetration of premixed pockets into the hot wake, hence enhancing the reaction in the premixed mode. Closer to the core of the wake a slower reaction occurs, dominated by a diffusive process.

The modeling approach employed here evaluates some of the modeling coefficients dynamically as a part of the solution. The fields of time-averaged c_v and Pr_t for the reacting flow are represented in Fig. 16. The variations of these closure coefficients are clearly associated with the shock and expansion pattern of the flow, but also show fluctuations along the shear layers, in the recirculation zone, and more downstream within the wake. As a consequence of the dynamic evaluation of Pr_t, the turbulent diffusivity is also locally adjusted to the local flow properties.

IV. Conclusions

A new hybrid numerical methodology that combines a smooth flow solver adapted to the resolution of turbulent vortical structures and a discontinuity-capturing upwind scheme is used to simulate shock/turbulence and shock/shear interactions using a LES approach. A new subgrid closure that explicitly provides closure for the compressible terms using a localized dynamic approach is applied to study turbulent mixing behind a model Scramjet strut injector under known operating conditions, and the predictions are compared with available experimental results. Overall, the agreement for both the nonreacting and reacting flow with measurements is reasonable. The results show that the hybrid solver captures unsteady shocks and shear turbulence in a consistent manner without requiring any ad hoc adjustments. Mixing in the nonreacting case is due to the unsteadiness and the high level of turbulence in the shear layers formed between the fuel jet and the freestream. In the reacting case, the flame is anchored by a recirculation region that occurs further downstream than in the immediate vicinity of the injectors. The radicals and hot products entrained into this recirculation are intermittently convected upstream and provide a preheating and ignition mechanism. Future studies will address these issues further, using a more sophisticated subgrid mixing model coupled to this new hybrid shock/turbulence capturing numerical methodology to alleviate some of the assumptions made in the present study.

Acknowledgments

This work was supported by the Air Force Office of Scientific Research (F. Fahroo, Program Manager) and computational support was provided by the Department of Defense high-performance computing centers at the Navy Supercomputing Resource Center and the Army Research Laboratory.

References

[1] Jameson, A., Schmidt, W., and Turkel, E., "Numerical Solution of the Euler Equations by Finite Volume Methods Using Runge–Kutta Time Stepping Schemes," AIAA Paper 81-1259, 1981.

[2] Ducros, F., Ferrand, V., Nicoud, F., Weber, C., Darracq, D., Gacherieu, C., and Poinsot, T., "Large-Eddy Simulation of the Shock/Turbulence Interaction," *Journal of Computational Physics*, Vol. 152, No. 2, 1999, pp. 517–549. doi:10.1006/jcph.1999.6238

[3] Cook, A. W., and Cabot, W. H., "Hyperviscosity for Shock-Turbulence Interactions," *Journal of Computational Physics*, Vol. 203, No. 2, 2005, pp. 379–385. doi:10.1016/j.jcp.2004.09.011

[4] Kawai, S., and Lele, S. K., "Localized Artificial Diffusivity Scheme for

Discontinuity Capturing on Curvilinear Meshes," *Journal of Computational Physics*, Vol. 227, No. 22, 2008, pp. 9498–9526. doi:10.1016/j.jcp.2008.06.034

[5] Adams, N. A., and Shariff, K., "A High-Resolution Hybrid Compact-ENO Scheme for Shock-Turbulence Interaction Problems," *Journal of Computational Physics*, Vol. 127, No. 1, 1996, pp. 27–51. doi:10.1006/jcph.1996.0156

[6] Vreman, B., "Direct and Large-Eddy Simulation of the Compressible Turbulent Mixing Layer," Ph.D. thesis, Univ. Twente, 1997.

[7] Pirozzoli, S., "Conservative Hybrid Compact-WENO Schemes for Shock-Turbulence Interaction," *Journal of Computational Physics*, Vol. 178, No. 1, 2002, pp. 81–117. doi:10.1006/jcph.2002.7021

[8] Hill, D. J., and Pullin, D. I., "Hybrid Tuned Center-Difference-WENO Method for Large Eddy Simulations in the Presence of Strong Shocks," *Journal of Computational Physics*, Vol. 194, No. 2, 2004, pp. 435–450. doi:10.1016/j.jcp.2003.07.032

[9] Génin, F., and Menon, S., "Studies of Shock/Turbulent Shear Layer Interaction Using Large-Eddy Simulation," *Computers and Fluids* (submitted for publication).

[10] Ristorcelli, J. R., "A Pseudo-Sound Constitutive Relationship for the Dilatational Covariances in Compressible Turbulence," *Journal of Fluid Mechanics*, Vol. 347, 1997, pp. 37–70. doi:10.1017/S0022112097006083

[11] Ristorcelli, J. R., and Blaisdell, G. A., "Consistent Initial Conditions for the DNS of compressible Turbulence," *Physics of Fluids A*, Vol. 9, No. 1, 1997, pp. 4–6. doi:10.1063/1.869152

[12] Dussauge, J.-P., "Compressible Turbulence of Supersonic Flows: Actions and Interactions," *Proceedings of the Symposium Turbulence and Interactions*, Porquerolles, France, May 29–June 02, 2006.

[13] Guerra, R., Waidmann, W., and Laible, C., "An Experimental Investigation of the Combustion of a Hydrogen Jet Injected Parallel in a Supersonic Air Stream," *AIAA 3rd International Aerospace Conference*, AIAA, Washington, D. C., 1991.

[14] Waidmann, W., Alff, F., Böhm, M., Clauß, W., and Oschwald, M., "Experimental Investigation of the Combustion Process in a Supersonic Combustion Ramjet (SCRAMJET)," DGLR Jahrestagung, Erlangen, Germany, 1994.

[15] Waidmann, W., Alff, F., Böhm, M., Brummund, U., Clauß, W., and Oschwald, M., "Supersonic Combustion of Hydrogen/Air in a Scramjet Combustion Chamber," *Space Technology*, Vol. 15, No. 6, 1995, pp. 421–429. doi:10.1016/0892-9270(95)00017-8

[16] Oevermann, M., "Numerical Investigation of Turbulent Combustion in a SCRAMJET Using Flamelet Modeling," *Aerospace Science and Technology*, Vol. 4, No. 7, 2000, pp. 463–480. doi:10.1016/S1270-9638(00)01070-1

[17] Génin, F., Chernyavsky, B., and Menon, S., "Large Eddy Simulation of Scramjet Combustion Using a Subgrid Mixing/Combustion Model," AIAA Paper 2003–7035, 2003.

[18] Berglund, M., and Fureby, C., "LES of Supersonic Combustion in a Scramjet Engine Model," *Proceedings of the Combustion Institute*, Vol. 31, No. 2, 2006, pp. 2497–2504.

[19] Zheng, Y., and Zou, J., "Partially Resolved Numerical Simulation for Supersonic Turbulent Combustion," AIAA Paper 2006-8040, 2006.

[20] Zhou, J.-F., Zheng, Y., and Liu, O.-Z., "Simulation of turbulent combustion in DLR Scramjet," *Journal of Zhejiang University (Science) A*, Vol. 8, No. 7, 2007, pp. 1053–1058. doi:10.1631/jzus.2007.A1053

[21] Gordon, S., and McBride, B. J., "Computer Program for Calculation of Complex Chemical Equilibrium Compositions and Applications," NASA Rept. No. 1311, 1994.

[22] Wilke, C. R., "A Viscosity Equation for Gas Mixtures," *Journal of Chemical Physics*, Vol. 18, No. 4, 1950, pp. 517–519. doi:10.1063/1.1747673

[23] Lesieur, M., Métais, O., and Comte, P., *Large-Eddy Simulations of Turbulence*, Cambridge Univ. Press, Cambridge, England, 2005.

[24] Garnier, E., Mossi, M., Sagaut, P., and Deville, M., "On the Use of Shock-Capturing for Large-Eddy Simulation," *Journal of Computational Physics*, Vol. 153, No. 2, 1999, p. 273. doi:10.1006/jcph.1999.6268

[25] Margolin, L. G., Rider, W. J., and Grinstein, F. F., "Modeling turbulent flow with implicit LES," *Journal of Turbulence*, Vol. 7, No. 15, 2006, pp. 1–27. doi:10.1080/14685240500331595

[26] Fureby, C., and Moller, S. I., "Large-Eddy Simulations of reacting flows applied to bluff-body stabilized flames," *AIAA Journal*, Vol. 33, No. 12, 1995, p. 2339. doi:10.2514/3.12989

[27] Veynante, D., and Poinsot, T., "Reynolds Averaged and Large Eddy Simulation Modelling for Turbulent Combustion," *New Tools in Turbulence Modelling*, edited by O. Metais, and J. Ferziger, Springer–Verlag, Heidelberg, Germany, 1996.

[28] Lee, S., Lele, S. K., and Moin, P., "Direct Numerical Simulation of Isotropic Turbulence Interacting with a Weak Shock Wave," *Journal of Fluid Mechanics*, Vol. 251, 1993, pp. 533–562. doi:10.1017/S0022112093003519

[29] Jamme, S., Cazalbou, J., Torres, F., and Chassaing, P., "Direct Numerical Simulation of the Interaction Between a Shock Wave and Various Types of Isotropic Turbulence," *Flow, Turbulence and Combustion*, Vol. 68, No. 3, 2002, pp. 227–268. doi:10.1023/A:1021197225166

[30] Chakravarthy, V., and Menon, S., "Modeling of Turbulent Premixed Flames in the Flamelet Regime," *Proceedings of First International Symposium on Turbulent and Shear Flow Phenomena*, edited by J. Eaton and S. Banerjee, Begell House, Redding, CT, 1999, pp. 189–194.

[31] Kim, W. W., Menon, S., and Mongia, H. C., "Large Eddy Simulations of a Gas Turbine Combustor Flow," *Combustion Science and Technology*, Vol. 143, Nos. 1–6, 1999, pp. 25–62. doi:10.1080/00102209908924192

[32] Liu, S., Meneveau, C., and Katz, J., "On the Properties of Similarity Subgrid-Scale Models as Deduced from Measurements in a Turbulent Jet," *Journal of Fluid Mechanics*, Vol. 275, 1994, pp. 83–119. doi:10.1017/S0022112094002296

[33] Lilly, D. K., "A Proposed Modification of the Germano Subgrid-Scale Closure Method," *Physics of Fluids A*, Vol. 4, No. 3, 1992, pp. 633–635. doi:10.1063/1.858280

[34] Moin, P., Squires, W., Cabot, W., and Lee, S., "A Dynamic Sub-grid Scale Model for Compressible Turbulence and Scalar Transport," *Physics of Fluids*, Vol. 3, No. 11, 1991, pp. 2746–2757. doi:10.1063/1.858164

[35] Menon, S., McMurtry, P., and Kerstein, A. R., "A Linear Eddy Mixing Model for Large Eddy Simulation of Turbulent Combustion," *LES of Complex Engineering and Geophysical Flows*, edited by B. Galperin and S. Orszag, Cambridge Univ. Press, Cambridge, England, 1993.

[36] Sankaran, V., and Menon, S., "Subgrid Combustion Modeling of 3-D Premixed Flames in the Thin Reaction-Zone Regime," *Proceedings of the Combustion Institute*, Vol. 30, No. 1, 2005, pp. 575–582. doi:10.1016/j.proci.2004.08.023

[37] Menon, S., and Patel, N., "Subgrid Modeling for Simulation of Spray Combustion in Large-Scale Combustors," *AIAA Journal*, Vol. 44, No. 4, 2006, pp. 709–723. doi:10.2514/1.14875

[38] Nelson, C. C., and Menon, S., "Unsteady Simulations of Compressible Spatial Mixing Layers," AIAA Paper 98-0786, 1998.

[39] Kim, D., and Kwon, J. H., "A High-Order Accurate Hybrid Scheme Using a Central Flux Scheme and a WENO Scheme for Compressible Flowfield Analysis," *Journal of Computational Physics*, Vol. 210, No. 2, 2005, pp. 554–583. doi:10.1016/j.jcp.2005.04.023

[40] Ukai, S., Génin, F., Srinivasan, S., and Menon, S., "Large Eddy Simulation of Reshocked Richtmyer–Meshkov Instability," AIAA Paper 2009-944, 2009.

[41] MacCormack, R. W., "The Effects of Viscosity in Hyper–Velocity Impact Cratering," AIAA Paper 69–354, 1969.

[42] Patel, N., Stone, C., and Menon, S., "Large-Eddy Simulation of Turbulent Flow over an Axisymmetric Hill," AIAA Paper 2003-0967, 2003.

[43] Sankaran, V., and Menon, S., "LES of Scalar Mixing in Supersonic Mixing Layers," *Proceedings of the Combustion Institute*, Vol. 30, No. 2, 2005, pp. 2835–2842. doi:10.1016/j.proci.2004.08.027

[44] Sankaran, V., and Menon, S., "Structure of Premixed Turbulent Flames in the Thin-Reaction-Zones Regime," *Proceedings of the Combustion Institute*, Vol. 28, No. 1, 2000, pp. 203–209.

[45] Eggenspieler, G., and Menon, S., "Large-Eddy Simulation of Pollutant Emission from DOE-HAT Combustor," *Journal of Propulsion and Power*, Vol. 20, No. 6, 2004, pp. 1076–1086. doi:10.2514/1.11427

[46] van Leer, B., "Towards the Ultimate Conservative Difference Scheme V. A Second Order Sequel to Godunov's Method," *Journal of Computational Physics*, Vol. 32, No. 1, 1979, pp. 101–136. doi:10.1016/0021-9991(79)90145-1

[47] Colella, P., and Woodward, P., "The Piecewise-Parabolic Method for Hydrodynamics," *Journal of Computational Physics*, Vol. 54, No. 1, 1984, pp. 174–201. doi:10.1016/0021-9991(84)90143-8

[48] Quirk, J. J., "A contribution to the great Riemann solver debate," *International Journal for Numerical Methods in Fluids*, Vol. 18, No. 6, 1994, pp. 555–574.
doi:10.1002/fld.1650180603

[49] Harten, A., Lax, P. D., and van Leer, B., "On Upstream Differencing and Godunov-Type Schemes for Hyperbolic Conservation Laws," *SIAM Review*, Vol. 25, No. 1, 1983, pp. 35–61.
doi:10.1137/1025002

[50] Toro, E. F., Spruce, M., and Speares, W., "Restoration of the Contact Surface in the HLL Riemann solver," *Shock Waves*, Vol. 4, No. 1, 1994, pp. 25–34.
doi:10.1007/BF01414629

[51] Einfeldt, B., "On Godunov-Type Methods for Gas Dynamics," *SIAM Journal on Numerical Analysis*, Vol. 25, No. 2, 1988, pp. 294–318.
doi:10.1137/0725021

[52] Masquelet, M., Génin, F., and Menon, S., "Update to the 107.leslie3d code for the SPEC MPI2007 benchmark," Georgia Inst. of Technology —Computational Combustion Lab., Rept. 2008-004-1, 2008.

[53] Lee, S., Lele, S. K., and Moin, P., "Interaction of Isotropic Turbulence with Shock Waves: Effect of Shock Strength," *Journal of Fluid Mechanics*, Vol. 340, 1997, pp. 225–247.
doi:10.1017/S0022112097005107

[54] Garnier, E., Sagaut, P., and Deville, M., "Large Eddy Simulation of Shock/Homogeneous Turbulence Interaction," *Computers and Fluids*, Vol. 31, No. 2, 2002, pp. 245–268.
doi:10.1016/S0045-7930(01)00022-6

[55] Edwards, J. R., "Numerical Simulations of Shock/Boundary Layer Interactions Using Time-Dependent Modeling Techniques: A Survey of Recent Results," *Progress in Aerospace Sciences*, Vol. 44, No. 6, 2008, pp. 447–465.
doi:10.1016/j.paerosci.2008.06.004

[56] Berglund, M., Fureby, C., Sabelnikov, V., and Tegnér, J., "On the Influence of Finite Rate Chemistry in LES of Self-Ignition in Hot Confined Supersonic Airflow," European Space Agency Special Rept. ESA SP-659, 2008.

[57] Rogers, R. C., and Chinitz, W., "On the Use of Hydrogen-Air Combustion Model in the Calculation of Turbulent Reacting Flows," AIAA Paper 82-0112, 1981.

[58] Mauss, F., Peters, N., Rogg, B., and Williams, F. A., "Reduced Kinetic Mechanisms for Premixed Hydrogen Flames," *Reduced Kinetic Mechanisms for Application in Combustion Systems*, edited by P. N. and, R. B., Lecture Notes in Physics, New series, Springer–Verlag, New York, 1993, p. 9.

[59] Eklund, D. R., Drummond, J. P., and Hassan, H. A., "Calculation of Supersonic Turbulent Reacting Coaxial Jets," *AIAA Journal*, Vol. 28, No. 9, 1990, pp. 1633–1641.
doi:10.2514/3.25262

[60] Baurle, R. A., and Girimaji, S. S., "Assumed PDF Turbulence–Chemistry Closure with Temperature Composition Correlations," *Combustion and Flame*, Vol. 134, Nos. 1–2, 2003, pp. 131–148.
doi:10.1016/S0010-2180(03)00056-7

[61] Masquelet, M., and Menon, S., "Large-Eddy Simulation of Flame-Turbulence Interactions in a $GH_2 - GO_2$ Shear Coaxial Injector," AIAA Paper 2008–5030, 2008.

[62] Amantini, G., Frank, J. H., Bennett, B. A. V., Smooke, M. D., and Gomez, A., "Comprehensive Study of the Evolution of an Annular Edge Flame During Extinction and Reignition of a Counterflow Diffusion Flame Perturbed by Vortices," *Combustion and Flame*, Vol. 150, No. 4, 2007, pp. 292–319.
doi:10.1016/j.combustflame.2007.04.010

F. Ladeinde
Associate Editor